Journal of Beijing Institute of Technology, 2026, Vol. 35, No. 5

Sparse Array MUSIC Based High-Resolution Passive Localization Method

Hang Liu, Yujie Fan✉, Yang Liu, Ziyu Zhao, Ruizhen Song, Shaobo Wang
(DFH Satellite Co., Ltd., Beijing 100094, China)

Abstract: The multiple signal classification (MUSIC) algorithm is a super-resolution technique whose angle estimation accuracy is fundamentally constrained by the signal-to-noise ratio (SNR) and the observation baselines. A higher SNR ensures a more stable partitioning of the noise subspace, while a greater number of observation baselines yield a larger equivalent synthesized SNR gain, thereby enhancing angle estimation precision. The angle estimation accuracy of traditional interferometric MUSIC processing is limited by the single-antenna received SNR and the number of receiving antennas per sub-aperture. To address this, this paper proposes a sparse array MUSIC based high-resolution passive localization method. This approach effectively integrates the physical gain of sparse array synthesis processing with the super-resolution capability of the MUSIC algorithm. By leveraging sparse array processing, the input conditions for the MUSIC algorithm are simultaneously improved in two dimensions: the observation matrix SNR and the observation baselines, which significantly enhances direction of arrival (DOA) estimation accuracy. Using a T-type sparse array configuration, this paper details the algorithmic derivation and simulations. Furthermore, a closed-form Cramér-Rao bound (CRB) expression for the sparse array MUSIC algorithm is derived, and simulation results are presented to compare the CRB performance of the proposed method against traditional MUSIC approaches.

Keywords: passive localization; sparse array; MUSIC algorithm; super-resolution; Cramér-Rao bound (CRB)

1 Introduction

In single-satellite direction-finding systems, array antennas are employed [1] to estimate the direction of arrival (DOA) of radiation sources. The estimation accuracy is inherently limited by factors such as the physical aperture of the array, the number of array elements, the signal-to-noise ratio (SNR), and the algorithmic capabilities. Traditional DOA estimation methods, such as amplitude comparison and interferometry, offer advantages in computational simplicity and real-time performance. However, their accuracy is constrained by the Rayleigh limit, rendering them incapable of resolving multiple signal sources within the same beamwidth. The advancement of array signal processing technology provides powerful tools to overcome these bottlenecks.

The multiple signal classification (MUSIC) algorithm achieves high-resolution DOA estimation by performing eigen-decomposition on the covariance matrix of the data received by the array, thereby separating signal subspace from noise subspace, followed by spectral peak searching within the noise subspace [1, 2]. Nevertheless, the practical DOA estimation accuracy of the MUSIC algorithm is not unconditionally guaranteed; it fundamentally depends on two core factors: the SNR of the observation matrix and the

Manuscript received Aug. 29, 2026; revised Sep. 10, 2026; accepted Sep. 15, 2026. The associate editor coordinating the review of this manuscript was Dr. Hao Huan.
✉ Corresponding author. Email: 18743052515@163.com
DOI: 10.15918/j.jbit1004-0579.2026.071

geometric configuration of the array. These two factors exhibit a multiplicative coupling relationship through the Cramér-Rao bound (CRB) [3].

$$\mathrm{CRB} \propto \frac{1}{\mathrm{SNR} * \sum_{k=1}^{K} (x_k^2 + y_k^2)} \tag{1}$$

This relationship clearly highlights the two critical constraints on MUSIC accuracy. First, the SNR determines the robustness of the subspace decomposition [4]. Under low SNR conditions, noise components dominate the covariance matrix, causing signal and noise eigenvalues to overlap. This prevents correct subspace partitioning and induces the threshold effect in the MUSIC algorithm, where DOA estimation errors increase drastically, potentially degrading performance below that of traditional methods. Only when the SNR exceeds a certain threshold can the signal and noise subspaces be effectively separated, allowing the algorithm to approach the CRB. Second, the array geometry dictates the sensitivity of the array manifold to angular variations [5]. Its physical essence is the sum of the squared lengths of all element pairs (virtual baselines). A more dispersed element distribution and larger spatial span result in a faster rate of change of the array manifold with respect to the angle, yielding sharper MUSIC spectral peaks and higher DOA estimation accuracy.

Sparse array technology addresses these limitations by sparsely distributing a small number of elements over a large spatial area. Through coherent processing of the signals received by each element, it simultaneously improves the input conditions for the MUSIC algorithm in both the SNR and array configuration dimensions. In the SNR dimension, sparse arrays achieve an M-fold increase in the observation matrix SNR via coherent accumulation of multi-element signals. This provides more favorable input conditions for accurate covariance matrix estimation and robust subspace decomposition, enabling the MUSIC algorithm to surpass the threshold and enter its normal operating region at lower raw SNRs [6, 7]. In the array configuration dimension, sparse array processing constructs a vast number of virtual observation baselines, improving upon traditional uniform arrays by tens or even hundreds of times. This geometric extension renders the array manifold highly sensitive to DOA variations, significantly reducing the CRB in accordance with the squared baseline relationship.

Addressing these issues, this paper proposes a sparse aperture MUSIC based high-resolution passive localization method. It systematically reveals the gain mechanism of sparse array synthesis processing on MUSIC algorithm performance from both the SNR and array configuration perspectives. A closed-form CRB expression for the sparse aperture MUSIC algorithm is derived, quantitatively characterizing the joint impact of SNR and virtual array baselines on DOA estimation accuracy. Finally, using a T-type array as an example, theoretical analysis and numerical simulations validate the effectiveness of the synergistic gain between sparse array synthesis processing and the MUSIC super-resolution algorithm.

2 Observation Modeling of Sparse Arrays

In passive reception scenarios, sparse arrays capture electromagnetic waves to obtain spatial spectrum sampling data on the antenna plane. A sparse array consists of several sparsely distributed small-aperture antennas. For analytical purposes, this paper utilizes a uniformly distributed T-type sparse array [8], the configuration of which is illustrated in Fig. 1.

The X and Y axes are orthogonal, sharing a central element. The Y-axis is uniformly distributed with $N+1$ elements, with an inter-element spacing of Δy and a baseline length of $D_y = N\Delta y$. The X-axis is uniformly distributed with $2M+1$ elements, with an inter-element

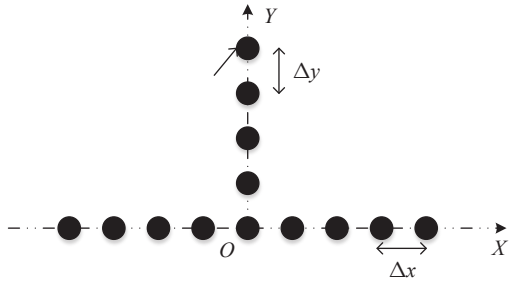


Fig. 1 Configuration of T-type sparse array

spacing of Δx and a baseline length of $D_x = 2M\Delta x$.

The observation scenario is depicted in Fig. 2, and the target is located at (x_0, y_0), transmitting a signal with a spectrum $S(f)$. The slant range from the target to the n-th sub-array of the sparse array is $R_{n,m}$, and the distance to the central sub-array is R_0. The elevation and azimuth angles of the incoming target signal are θ and φ, respectively.

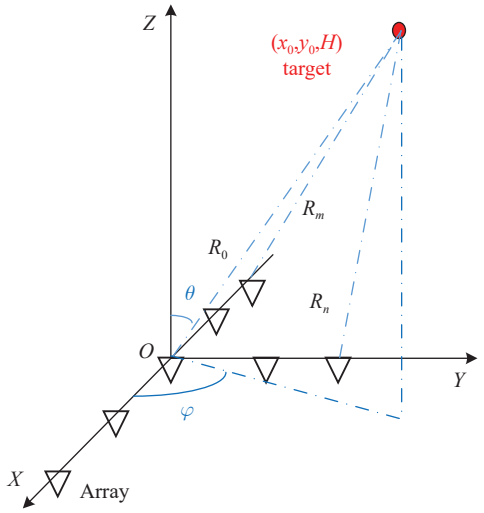


Fig. 2 Observation scenario

All sub-arrays of the sparse antenna receive signals simultaneously to acquire sampled data. The signal sampling result obtained by the m-th sub-array along the X-axis is $x_m(t)$, $m = -M$, $-M+1$, $\cdots$, M, and the signal sampling result obtained by the n-th antenna along the azimuth (Y-axis) is $y_n(t)$, $n = 0, 1, \cdots, N$. Arranged sequentially according to the X and Y element distributions, the signal vectors are formed as

$$\begin{aligned} \boldsymbol{x} &= [x_{-M}(t);\ x_{-M+1}(t);\ \cdots;\ x_M(t)] \\ \boldsymbol{y} &= [y_0(t);\ y_1(t);\ \cdots;\ y_N(t)] \end{aligned} \tag{2}$$

Applying the Fourier transform to the signal vector yields the signal frequency-domain vector.

$$\begin{aligned} \boldsymbol{X} &= [x_{-M}(f);\ x_{-M+1}(f);\ \cdots;\ x_M(f)] \\ \boldsymbol{Y} &= [y_N(f);\ y_{N-1}(f);\ \cdots;\ y_0(f)] \\ x_n &= S(f)\exp\left(-\mathrm{j}2\pi f_c\frac{R_n}{c}\right) \\ y_m &= S(f)\exp\left(-\mathrm{j}2\pi f_c\frac{R_m}{c}\right) \end{aligned} \tag{3}$$

Conjugate multiplication of the X-axis and Y-axis signal frequency-domain vectors generates the observation matrix.

$$\boldsymbol{V} = \boldsymbol{Y}\boldsymbol{X}' = \begin{bmatrix} v_{N,-M} & v_{N,-M+1} & \cdots & v_{N,M-1} & v_{N,M} \\ \cdots & \cdots & \cdots & \cdots & \cdots \\ v_{0,-M} & v_{N,-M+1} & \cdots & v_{N,M-1} & v \end{bmatrix} \tag{4}$$

The phase of each element v_{nm} in the observation matrix represents the phase difference between the n-th sub-array $G_n(x_n, y_n)$ on the Y-axis and the m-th sub-array $G_m(x_m, y_m)$ on the X-axis, expressed as

$$\begin{aligned} v_{nm} &= \sum_{f=f_1}^{f_2} y_n(f)\,x_m(f) = \\ &\sum_{f=f_1}^{f_2} S(f)\,S^*(f)\exp\left[-\mathrm{j}\frac{2\pi f_c}{c}(R_n - R_m)\right] = \\ &\sum_{f=f_1}^{f_2} ||S(f)||^2\exp\left[-\mathrm{j}\frac{2\pi f_c}{c}(R_n - R_m)\right] \end{aligned} \tag{5}$$

This processing evidently yields an energy gain within the target frequency band. T denotes the signal duration for this processing; $||S(f)||^2$ can be approximated as a rectangular function of width $B = f_2 - f_1$. This is equivalent to performing a discrete Fourier fransform (DFT) on the rectangular function, which can be approximated as

$$A = \sum_{f=f_1}^{f_2} ||S(f)||^2 \approx \sqrt{BT} \tag{6}$$

When the sparse array dimensions satisfy the far-field condition $D_{x,y} << R_{n,m}$, the path difference of the received signals between sub-arrays can be expressed as

$$\begin{aligned} R_{n,m} \approx & R_0 - x_{n,m}\sin\theta\cos\varphi - y_{n,m}\sin\theta\sin\varphi \\ \Delta R_{nm} = & R_n - R_m \approx \\ & (x_m - x_n)\sin\theta\cos\varphi + (y_m - y_n)\sin\theta\sin\varphi \end{aligned} \tag{7}$$

Consequently, v_{nm} is formulated as

$$\begin{aligned} v_{nm} = & A\exp\{-\mathrm{j}\Delta\phi_{nm}\} \\ \Delta\phi_{nm} = & \frac{2\pi f_c}{c}[(x_m - x_n)\sin\theta\cos\varphi + \\ & (y_m - y_n)\sin\theta\sin\varphi] \end{aligned} \tag{8}$$

This equation indicates that the phase difference $\Delta\phi_{nm}$ between $G_n(x_n, y_n)$ and $G_m(x_m, y_m)$ is equivalent to the phase difference between an element located at $[x_n - x_m, \mathrm{y}_n - y_m]$ and an element at the origin. In other words, a virtual sub-arr G_{nm} is formed at $[x_n - x_m, \mathrm{y}_n - y_m]$, receiving a signal v_{nm}. Thus, the T-type array can be expanded into a rectangular array with $(2M+1)*(N+1)$ sub-arrays. Here, v_{nm} is the coherent result of the received signals from the sub-array G_{nm} and the sub-array at the origin G_{00}, and the phase $\Delta\phi_{nm}$ is the phase difference between G_{nm} and the G_{00}.

Evidently, the observation matrix $\boldsymbol{v}_{nm}$ strictly satisfies Hermitian symmetry.

$$\boldsymbol{v}_{n,m} = \boldsymbol{v}^*_{-n,-m} \tag{9}$$

From this, the observed value of $n = -N$, $-N+1, \cdots, -1$ can be obtained, yielding an equivalent rectangular array of $(2N+1)*(2M+1)$ sub-arrays. The observation matrix for the equivalent rectangular array is expressed as

$$\boldsymbol{V} = \begin{bmatrix} v_{N,-M} & v_{N,-M+1} & \cdots & v_{N,M-1} & v_{N,M} \\ \cdots & \cdots & \cdots & \cdots & \cdots \\ v_{0,-M} & v_{N,-M+1} & \cdots & v_{N,M-1} & v_{N,M} \\ v_{-1,-M} & v_{-1,-M+1} & \cdots & v_{-1,M-1} & v_{-1,M} \\ \cdots & \cdots & \cdots & \cdots & \cdots \\ v_{-N,-M} & v_{-N,-M+1} & \cdots & v_{-N,M-1} & v_{-N,M} \end{bmatrix} = \begin{bmatrix} v_{N,-M} & v_{N,-M+1} & \cdots & v_{N,M-1} & v_{N,M} \\ \cdots & \cdots & \cdots & \cdots & \cdots \\ v_{0,-M} & v_{N,-M+1} & \cdots & v_{N,M-1} & v_{N,M} \\ v^*_{1,M} & v^*_{1,M-1} & \cdots & v^*_{1,-M+1} & v^*_{1,-M} \\ \cdots & \cdots & \cdots & \cdots & \cdots \\ v^*_{N,M} & v^*_{N,M-1} & \cdots & v^*_{N,-M+1} & v^*_{N,-M} \end{bmatrix} \tag{10}$$

Through sparse array processing, a large-aperture antenna can be equivalently constructed using a small number of antennas. This approach equivalently increases the number of phase measurement points obtained from the virtual array elements. Specifically, the observation baselines are expanded from max $N+2M+1$ to $(2M+1)*(2N+1)$. The spatial coverage of the virtual array elements spans twice the baseline length of the physical aperture array, and the *Y*-axis observation baseline length is extended from $D_y = N\Delta y$ to $D_y = 2N\Delta y$. Considering that angular resolution is inversely proportional to the physical size of the array $\theta \approx k\lambda/D$, the DOA estimation accuracy along the *Y*-axis can be improved by a factor of 2 compared to traditional interferometric direction-finding methods. Furthermore, sparse array synthesis achieves coherent accumulation of the $N+2M+1$ element gain while acquiring inter-channel coherent accumulation gain $A = \sqrt{BT}$. The substantial increase in signal SNR can effectively enhance localization accuracy of the system. Furthermore, sparse array processing increases the spatial degrees of freedom, enabling the separation of multiple simultaneous co-frequency signals via angular resolution cells. For a sparse array composed of $N+2M+1$ subarrays, it is capable of resolving up to $N+2M$ such signals.

3 Super-Resolution Localization Method Based on Spatial Smoothing MUSIC

Sparse array processing enhances the DOA estimation accuracy by extending the observation baselines and significantly boosting the SNR of the observed signals. This makes it highly suitable for spatial smoothing MUSIC methods, which are sensitive to SNR, to achieve super-resolution DOA estimation.

To ensure the capability to resolve multiple targets, assuming a resolution capability for I

targets, the observation matrix of the MUSIC algorithm must possess at least $I+1$ linearly independent observation columns [9]. A sliding window process is applied to the interferometric measurement matrix, with a window length of $(2N-Idn)\,(2M-Idm)$ and sliding steps of dn and dm along the X and Y axes, respectively. Performing $I+1$ sliding window operations yields $I+1$ interferometric measurement matrices $\boldsymbol{V}_i$, as illustrated in Fig. 3. In this method, to ensure that each observation vector has a sufficient number of observations, the window length must be large enough and must satisfy $I \leqslant \min\{2N, 2M\}$. Consequently, compared with the original sparse array processing, this approach suffers from a reduced capability for multi-target separation.

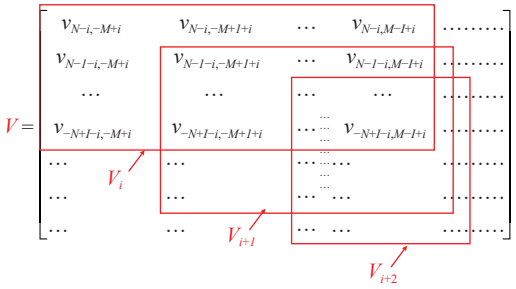


Fig. 3 Division method of interferometric measurement matrix

Since $\boldsymbol{V}_i$ and $\boldsymbol{V}_{i+1}$ correspond to identical virtual aperture configurations, differing only by a global translation of dm and dn along the X and Y axes, the phase difference $\Delta\phi$ between them is approximately a constant. Therefore, the $\boldsymbol{V}_i$ interferometric measurement matrices can share the same steering vector.

$$\begin{aligned}\Delta\phi =& 2\pi f_c[dn * \Delta y * \sin\theta\cos\varphi + \\ & dm * \Delta x * \sin\theta\sin\varphi]\end{aligned} \tag{11}$$

The i-th interferometric measurement matrix $\boldsymbol{V}_i$ consists of $2M+1-I$ column vectors, expressed as

$$\boldsymbol{V}_i = [\vec{v}_1,\ \vec{v}_2,\ \ldots,\ \vec{v}_{2M+1-I}] = \begin{bmatrix} v_{N-i,-M+i} & v_{N-i,-M+1+i} & \cdots & v_{N-i,M-I+i} \\ v_{N-1-i,-M+i} & v_{N-1-i,-M+1+i} & \cdots & v_{N-1-i,M-I+i} \\ \cdots & \cdots & \cdots & \cdots \\ v_{-N+I-i,-M+i} & v_{-N+I-i,-M+1+i} & \cdots & v_{-N+I-i,M-I+i} \end{bmatrix} \tag{12}$$

Considering that the sub-arrays of the T-type array are located on the X and Y axes, the virtual sub-array positions corresponding to the interferometric measurement matrix $\boldsymbol{G}_i$ are

$$\boldsymbol{G}_i = \begin{bmatrix} (x_{-M+i}, \mathrm{y}_{N-i}) & (x_{-M+1+i}, \mathrm{y}_{N-i}) & \cdots & (x_{M-I+i}, \mathrm{y}_{N-i}) \\ (x_{-M+i}, \mathrm{y}_{N-1-i}) & (x_{-M+1+i}, \mathrm{y}_{N-1-i}) & \cdots & (x_{M-I+i}, \mathrm{y}_{N-1-i}) \\ \cdots & \cdots & \cdots & \cdots \\ (x_{-M+i}, \mathrm{y}_{-N+I-i}) & (x_{-M+i}, \mathrm{y}_{-N+I-i}) & \cdots & (x_{M-I+i}, \mathrm{y}_{-N+I-i}) \end{bmatrix} \tag{13}$$

The signal model corresponding to each sub-array position $\boldsymbol{G}_i$ in the equivalent virtual array is expressed as

$$a(x, \mathrm{y}, \xi, \eta) = \exp\left(-\mathrm{j}\frac{2\pi f_c}{c}(x\xi + y\eta)\right) \tag{14}$$

$$\xi = \sin\theta\cos\varphi \qquad \eta = \sin\theta\sin\varphi$$

By substituting the position of each sub-array $\boldsymbol{G}_i$ and calculating the signal value corresponding to each virtual sub-array position sequentially, the steering matrix is obtained

$$\boldsymbol{A}(\xi,\eta) = [\vec{a}_1, \vec{a}_2, \cdots, \vec{a}_{2M+1-I}] = \begin{bmatrix} a(x_{-M+i}, \mathrm{y}_{N-i}, \xi, \eta) & a(x_{-M+1+i}, \mathrm{y}_{N-i}, \xi, \eta) & \cdots & a(x_{M-I+i}, \mathrm{y}_{N-i}, \xi, \eta) \\ a(x_{-M+i}, \mathrm{y}_{N-1-i}, \xi, \eta) & a(x_{-M+1+i}, \mathrm{y}_{N-1-i}, \xi, \eta) & \cdots & a(x_{M-I+i}, \mathrm{y}_{N-1-i}, \xi, \eta) \\ \cdots & \cdots & \cdots & \cdots \\ a(x_{-M+i}, \mathrm{y}_{-N+I-i}, \xi, \eta) & a(x_{-M+i}, \mathrm{y}_{-N+I-i}, \xi, \eta) & \cdots & a(x_{M-I+i}, \mathrm{y}_{-N+I-i}, \xi, \eta) \end{bmatrix} \tag{15}$$

Vectorizing the interferometric measurement matrix $\vec{\boldsymbol{V}}_i$ yields the observation vector

$$\vec{\boldsymbol{V}}_i = [\vec{v}_1; \vec{v}_2; \cdots; \vec{v}_{2M+1-I}] \tag{16}$$

The final observation matrix is constructed as

$$\overline{\boldsymbol{V}} = \left[\vec{\boldsymbol{V}}_0, \vec{\boldsymbol{V}}_1, \cdots, \vec{\boldsymbol{V}}_I\right] \tag{17}$$

The covariance matrix $\boldsymbol{R} = \overline{\boldsymbol{V}}\overline{\boldsymbol{V}}^{\mathrm{T}}$ is computed, and eigen-decomposition is performed on

$\boldsymbol{R}$ to obtain I+1 eigenvalues λ_i and their corresponding eigenvectors $\boldsymbol{U}_i$, arranged in descending order of their eigenvalues. The number of signals I_0 is determined using the minimum description length (MDL) criterion for subspace partitioning [10]. The first I_0 eigenvectors form the signal subspace, while the remaining eigenvectors constitute the noise subspace

$$\begin{aligned} \boldsymbol{U}_n &= [\boldsymbol{U}_{I_0}, \boldsymbol{U}_{I_0+1}, \boldsymbol{U}_i, \cdots, \boldsymbol{U}_I] \\ i &= I_0 + 1, \cdots, I \end{aligned} \tag{18}$$

The steering matrix is vectorized to construct the steering vector

$$\overrightarrow{\boldsymbol{A}}(\xi, \eta) = [\overrightarrow{a}_1; \overrightarrow{a}_2; \cdots; \overrightarrow{a}_{2M+1-I}] \tag{19}$$

The field of view is discretized into a grid (ξ, η), and the projection of the steering vector onto the noise subspace is calculated to obtain the target spatial spectrum $P_m(\xi, \eta)$. Spectral peak searching is then performed to determine the DOA parameters (ξ, η) of the target

$$P_m(\xi, \eta) = \frac{1}{\overrightarrow{\boldsymbol{A}}(\xi, \eta)^H \boldsymbol{U}_n \boldsymbol{U}_n{}^H \overrightarrow{\boldsymbol{A}}(\xi, \eta)} \tag{20}$$

4 Localization Accuracy Analysis

The proposed method achieves the synthesis of array gain for $2M + N + 1$ sub-arrays through sparse synthetic processing. Additionally, it acquires inter-channel coherent accumulation gain $A = \sqrt{BT}$. Consequently, the SNR of the processed observation matrix is significantly enhanced compared to the raw signal SNR, and the number of observation baselines is increased from max $2M + N + 1$ to $(2M + 1)(2N + 1)$. Since spatial spectrum estimation algorithms like MUSIC are highly sensitive to SNR, this processing substantially improves the Cramér-Rao Bound (CRB) of DOA estimation accuracy compared to the traditional interferometric MUSIC method. The CRB formula for the DOA estimation accuracy of the MUSIC algorithm is given by

$$\begin{aligned} \mathrm{CRB}_\varphi &= \frac{\lambda^2}{8\pi^2 N * \mathrm{SNR} * \cos^2\theta \left(\sin^2\varphi \sum_{k=1}^{K} x_k^2 + \cos^2\varphi \sum_{k=1}^{K} y_k^2 \right)} \\ \mathrm{CRB}_\theta &= \frac{\lambda^2}{8\pi^2 N * \mathrm{SNR} * \sin^2\theta \left(\cos^2\varphi \sum_{k=1}^{K} x_k^2 + \sin^2\varphi \sum_{k=1}^{K} y_k^2 \right)} \end{aligned} \tag{21}$$

Comparing the CRB of DOA estimation accuracy between the traditional interferometric MUSIC and the sparse array MUSIC algorithms under identical baseline lengths reveals that the SNR of the observation matrix obtained via sparse array processing is $A(2M + N + 1)$ times that of the raw signal, and the number of observation baselines K is also times greater. Therefore, the DOA estimation accuracy of the sparse array MUSIC method is evidently superior to that of the traditional interferometric MUSIC method.

5 Simulation Verification

Simulations were conducted to validate the proposed algorithm using a T-type array. Fifty sub-arrays are uniformly spaced along the X-dimension, and 100 sub-arrays are uniformly spaced along the Y-dimension, sharing a central antenna located at coordinates $(0, 0)$ with an inter-element spacing of $\Delta x, y = 0.2\ m$.

Nine target points are uniformly distributed in the scenario, transmitting signals with the same frequency and waveform. A linear frequency modulated (LFM) signal is employed with a carrier frequency of 5 GHz, a bandwidth of 1 MHz, a pulse width of 100 μs, and a time-domain amplitude of 1. The single-channel SNR is 15 dB. The target points are distributed on the $z = 500$ km plane, with their positional parameters detailed in Tab. 1.

Tab. 1 True positions of targets

Target point	Coordinates (km)	Target point	Coordinates (km)
1	(15, -15)	6	(0, 15)
2	(15, 0)	7	(15, 15)
3	(15, 15)	8	(-15, 0)
4	(0, -15)	9	(-15, 15)
5	(0, 0)	-	-

Assuming an ideal receiver where the system bandwidth exceeds the signal bandwidth, the system receives the signal and directly performs sparse aperture processing. The localization results are shown in Fig. 4, and a slice of the target localization points is presented in Fig. 5. The unambiguous range is $\xi_{\max} - \xi_{\min} = 0.3$, corresponding to an unambiguous angular field of view of $(-8.6^{\circ}) - 8.6^{\circ}$. The resolution cell size is $\Delta\xi = \Delta\eta = 2\lambda_c / D_x = 0.012$, and the corresponding DOA estimation accuracy is approximately $\mathrm{d}\theta, \varphi \approx 0.7^{\circ}$.

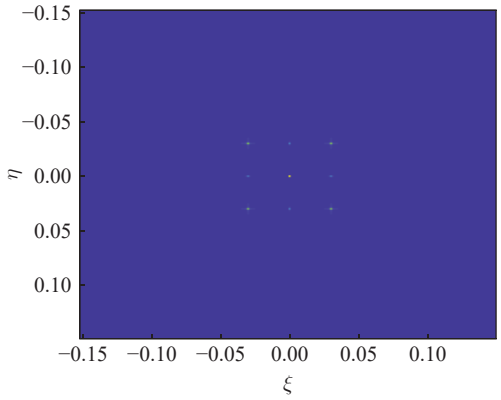


Fig. 4 Localization distribution of sparse aperture

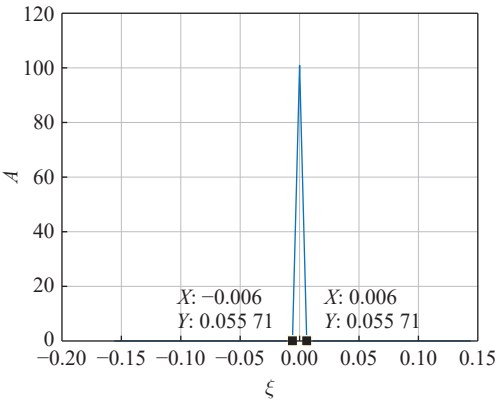


Fig. 5 Target localization result slice of sparse aperture processing

Applying the proposed method generates an equivalent array with 100×100 virtual elements. Setting the sliding window step to 1 and the window length to 90 yields 11 observation windows. Constructing the observation matrix and completing the localization processing produces the localization distribution map shown in Fig. 6, with a target localization slice in Fig. 7. The resolution cell size is $\Delta\xi = \Delta\eta = 2\lambda_c / D_x = 0.006$, and the DOA estimation accuracy is significantly superior to the direct sparse aperture processing method.

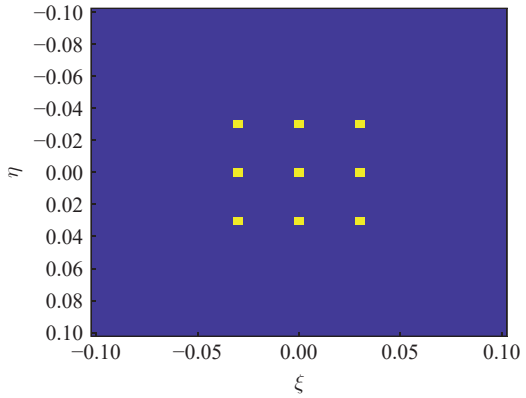


Fig. 6 Localization distribution of sparse aperture MUSIC

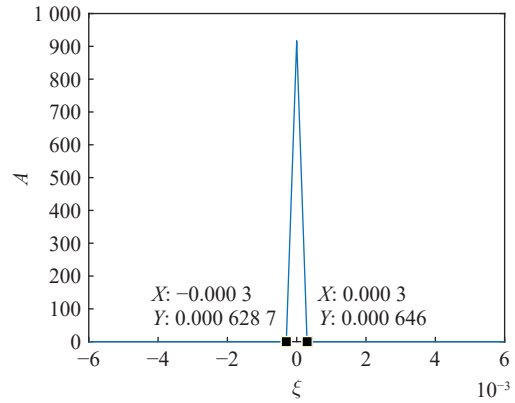


Fig. 7 Target localization result slice of sparse aperture MUSIC

Monte Carlo simulation experiments were conducted, in which 100 consecutive sampling slices were used for 100 localization processing runs, with each slice lasting 100 μs. The angle measurement accuracy is evaluated using the root mean square error (RMSE) between the measured values and the true values. A compari-

son of the DOA estimation accuracy between the interferometric MUSIC and the sparse array MUSIC under this baseline is presented in Fig. 8. The results demonstrate that the sparse array MUSIC method yields a significant improvement in DOA estimation accuracy compared to the traditional interferometric MUSIC approach.

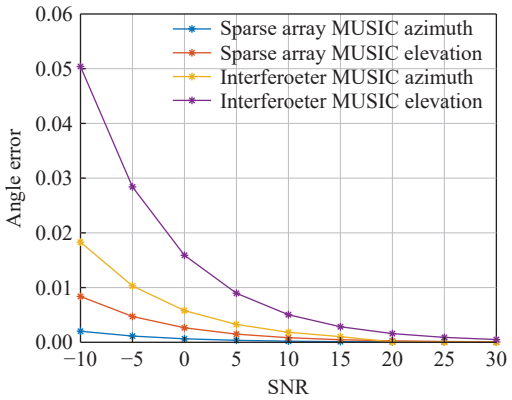


Fig. 8 Comparison of angle estimation accuracy between interferometric MUSIC and sparse array MUSIC

6 Conclusion

This paper proposes a high-resolution passive localization method based on sparse array MUSIC. This approach effectively integrates the physical gain of sparse array synthesis processing with the super-resolution capability of the MUSIC algorithm. By utilizing sparse array processing, the input conditions for the MUSIC algorithm are simultaneously improved in terms of both the SNR of the observation matrix and the observation baseline, thereby achieving a significant enhancement in direction-finding accuracy.

Taking the T-shaped sparse array as a specific configuration, this paper derives the processing method for sparse array MUSIC and provides a closed-form expression for the CRB. Through theoretical analysis and simulation verification, it is demonstrated that, under identical single-channel SNR conditions, the proposed method outperforms the conventional interferometric MUSIC algorithm.

References:

[1] H. Huang, W. Yuan and A. Nallanathan,"Sensing mobile targets in near-field ISAC systems: a low complexity modified MUSIC approach," *IEEE Transactions on Vehicular Technology*, vol. 74, no. 12, pp. 19887-19891, 2025.

[2] J. Liang and D. Liu,"Passive localization of mixed near-field and far-field sources ssing two-stage MUSIC algorithm," *IEEE Transactions on Signal Processing*, vol. 58, no. 1, pp. 108-120, 2010.

[3] P. Kulkarni and P. P. Vaidyanathan, "On the efficiency of a Toeplitz covariance matrix construction approach for DOA estimation," in *2025 59th Asilomar Conference on Signals, Systems, and Computers*, Pacific Grove, CA, USA, pp. 1719-1723, 2025.

[4] H. Xu, T. Wu, Y. Tian, K. Zhi, W. Liu, B. Liu, H. C. So, N. Al-Dhahir, K. F. Tong, C. B. Chae, and K. K. Wong,"Fluid antenna enabled direction-of-arrival estimation under time-constrained mobility," *IEEE Transactions on Communications*, vol. 74, pp. 9108-9124, 2026.

[5] M. Wang and A. Nehorai,"Coarrays, MUSIC, and the Cramér–Rao bound," *IEEE Transactions on Signal Processing*, vol. 65, no. 4, pp. 933-946, 2017.

[6] Y. Li, C. Zhang, H. Liu, J. Wu, X. Zhang, A. Liu, G. Song, Y. Li, D. Zhu, and X. Yao, "An airborne C-band one-dimensional microwave interferometric radiometer with ocean aviation experimental results," *IEEE Transactions on Geoscience and Remote Sensing*, vol. 60, pp. 1-16, 2022.

[7] T. Zheng, F. Hu, H. Hu and P. Fu,"Channel compressive aperture synthesis," *IEEE Geoscience and Remote Sensing Letters*, vol. 17, no. 6, pp. 1027-1031, 2020.

[8] S. Du, F. Zhao, X. Chen, J. He, X. Chen and L. Jiang, "A new layout of wide swath synthetic aperture array, " in *2022 3rd China International SAR Symposium (CISS)*, pp. 1-7, 2022.

[9] Z. Fang and Z. Luo, "A highly robust super-resolution range-velocity processing algorithm for multi-target scenarios in OFDM integrated sensing and communications, " in *ICC 2024 - IEEE International Conference on Communications*, pp. 1201-1207, 2024.

[10] J. Zhao, R. Gui and X. Dong,"PHD filtering for multi-source DOA rracking with extended co-prime array: an improved MUSIC pseudo-likelihood," *IEEE Communications Letters*, vol. 25, no. 10, pp. 3267-3271, 2021.



Hang Liu is an associate professor at the DFH Satellite Co., Ltd. His research focuses on spaceborne passive localization.



Ziyu Zhao is a researcher at the DFH Satellite Co., Ltd. Her research focuses on spaceborne passive localization.



Yujie Fan is a researcher at the DFH Satellite Co., Ltd. Her research interests include spaceborne passive localization and synthetic aperture radar (SAR) imaging.



Ruizhen Song is a researcher at the DFH Satellite Co., Ltd. Her research focuses on spaceborne passive localization.



Yang Liu is an associate professor at the DFH Satellite Co., Ltd. His research focuses on spaceborne passive localization.



Shaobo Wang is a professor at the DFH Satellite Co., Ltd. His research focuses on spaceborne passive localization.